Magma Chamber Response to Ice Unloading: Applications to Volcanism in the West Antarctic Rift System

Allie N. Coonin[1], Christian Huber[1], Juliana Troch[2], Meredith Townsend[3], Kathryn J Scholz[4], and Bradley S Singer[5]

[1]Brown University
[2]RWTH Aachen University
[3]Lehigh University
[4]University of Oregon
[5]University of Wisconsin-Madison

July 15, 2024

Abstract

While the effects of volcanism on Earth's climate are well understood, the volcano-ice sheet system hosts a two-way feedback. Volcanic activity promotes ice melting, which in turn affects the internal dynamics of the magma chamber below. At present, accurate forecasts of sea-level rise hinge on the stability of the West Antarctic Ice Sheet, and thus require consideration of subglacial volcano-deglaciation feedbacks. The West Antarctic Ice Sheet, grounded below sea-level, is particularly vulnerable to collapse, yet its position atop an active volcanic rift is seldom considered. Ice unloading raises the geotherm and alters the crustal stress field, impacting dike propagation. However, the consequences on internal magma chamber dynamics and thus long-term eruption behavior remain elusive. Given potential for unloading-triggered volcanism in West Antarctica to accelerate ice retreat, we adapt the thermomechanical magma chamber model of Scholz et al. (2023) for West Antarctic Rift basalts, simulating a shrinking ice load through a prescribed decrease of lithostatic pressure. Examining different unloading scenarios, we investigate the impacts on volatile partitioning within the magma and eruptive trajectory across a wide range of initial magma chamber conditions. Pressurization of a magma chamber beyond a critical threshold results in eruption, delivering enthalpy to the ice. Considering the removal of km-thick ice sheets, we demonstrate the rate of unloading is dominant in influencing the cumulative mass erupted and consequently, heat released to the ice. These findings provide fundamental insights into the complex volcano-ice interactions in West Antarctica and other subglacial volcanic settings.

Hosted file

`Coonin_main_text_final.docx` available at https://authorea.com/users/800926/articles/1182631-magma-chamber-response-to-ice-unloading-applications-to-volcanism-in-the-west-antarctic-rift-system

Hosted file

`Coonin_supplements_final.docx` available at https://authorea.com/users/800926/articles/1182631-magma-chamber-response-to-ice-unloading-applications-to-volcanism-in-the-west-antarctic-rift-system

Magma Chamber Response to Ice Unloading: Applications to Volcanism in the West Antarctic Rift System

A. N. Coonin[1*], C. Huber[1], J. Troch[2], M. Townsend[3], K. Scholz[4], and B. S. Singer[5]

[1]Department of Earth, Environmental, and Planetary Sciences, Brown University, Providence, RI, 02912, USA

[2]Division of Earth Sciences and Geography, RWTH Aachen University, Bunsenstrasse 8, 52072 Aachen, Germany

[3]Department of Earth and Environmental Sciences, Lehigh University, Bethlehem, PA, 18015, USA

[4] Department of Earth Sciences, University of Oregon, Eugene, OR, 97403, USA

[5] Department of Geoscience, University of Wisconsin-Madison, Madison, WI, 53706, USA

*Corresponding author: Allie N. Coonin (allie_coonin@brown.edu)

Key Points:

- During deglaciation, the evolution of a magma chamber beneath several kilometers of ice is sensitive to the rate at which ice is removed.
- A critical rate of unloading can trigger additional eruption events.
- Ice unloading expedites the onset of volatile exsolution, with consequences for magma chamber pressurization and eruption size.

Abstract

While the effects of volcanism on Earth's climate are well understood, the volcano-ice sheet system hosts a two-way feedback. Volcanic activity promotes ice melting, which in turn affects the internal dynamics of the magma chamber below. At present, accurate forecasts of sea-level rise hinge on the stability of the West Antarctic Ice Sheet, and thus require consideration of subglacial volcano-deglaciation feedbacks. The West Antarctic Ice Sheet, grounded below sea-level, is particularly vulnerable to collapse, yet its position atop an active volcanic rift is seldom considered. Ice unloading raises the geotherm and alters the crustal stress field, impacting dike propagation. However, the consequences on internal magma chamber dynamics and thus long-term eruption behavior remain elusive. Given potential for unloading-triggered volcanism in West Antarctica to accelerate ice retreat, we adapt the thermomechanical magma chamber model of Scholz et al. (2023) for West Antarctic Rift basalts, simulating a shrinking ice load through a prescribed decrease of lithostatic pressure. Examining different unloading scenarios, we investigate the impacts on volatile partitioning within the magma and eruptive trajectory across a wide range of initial magma chamber conditions. Pressurization of a magma chamber beyond a critical threshold results in eruption, delivering enthalpy to the ice. Considering the removal of km-thick ice sheets, we demonstrate the rate of unloading is dominant in influencing the cumulative mass erupted and consequently, heat released to the ice. These findings provide fundamental insights into the complex volcano-ice interactions in West Antarctica and other subglacial volcanic settings.

Plain Language Summary

In regions like West Antarctica, volcanic eruptions occur underneath ice sheets. When hot magma comes in contact with ice, it can accelerate the melting of the ice cover. Beyond this, as climate change causes ice sheets to shrink, the decreasing weight on a volcano may affect its likelihood of erupting. The effects of ice loss above volcanoes on the underlying volcanic activity are not yet well understood. We conducted computer simulations to explore how gradual ice loss affects magma stored in the Earth's crust. We find that volcanoes beneath shrinking ice sheets are sensitive to the rate at which the ice sheet is shrinking. As the ice melts away, the reduced weight on the volcano allows the magma to expand, applying pressure upon the surrounding rock that may facilitate eruptions. Additionally, the reduced weight from the melting ice above also allows dissolved water and carbon dioxide to form gas bubbles, which causes pressure to build up in the magma chamber and may eventually trigger an eruption. Under these conditions, we find that the removal of an ice sheet above a volcano results in more abundant and larger eruptions, which may hasten the melting of overlying ice through complex feedback mechanisms.

1 Introduction

The ongoing stability of the West Antarctic Ice Sheet plays a crucial role in predictions of modern sea-level rise. One of Earth's largest reservoirs of land ice, the West Antarctic Ice Sheet is particularly vulnerable to collapse as its margins are grounded below sea-level (marine-based). As sea-level rises, such a marine-based ice sheet becomes increasingly submerged, accelerating the retreat of the grounding line (Gomez et al., 2020). Additionally, portions of the West

Antarctic Ice Sheet above sea-level rest on bedrock that slopes downward, promoting ice loss to the ocean (Fretwell et al., 2013; Van Wyk de Vries et al., 2018). Factors affecting the stability of the West Antarctic Ice Sheet include atmospheric CO_2 emissions (e.g. Sutter et al., 2023), glacial isostatic adjustment and grounding line dynamics (e.g. Gomez et al. 2015; Barletta et al., 2018), ice shelf melting and calving due to interaction with a warming ocean (e.g. Stevens et al., 2020), and bedrock geometry. While various studies investigate these parameters, one often overlooked factor is the potential for feedback with volcanism.

The West Antarctic Ice Sheet sits atop a partially hidden, complex network of active rifts known as the West Antarctic Rift System (WARS). The WARS comprises one of Earth's largest volcanic provinces, with more than 100 eruptive centers thought to be currently active, some exposed and some subglacial (LeMasurier et al. 1990; Smellie & Edwards, 2016, Van Wyk de Vries, 2018). While eruptions from kilometers-deep subglacial magmatic systems may not be directly observed, digital elevation models utilizing ice-penetrating radar indicate intact subglacial volcanic cones (Behrendt et al., 2002; Corr & Vaughan, 2008; Schroeder et al., 2014; Van Wyk de Vries, 2018). Given that rifting in West Antarctica initiated around 66 Ma and glaciation began around 34 Ma, the presence of intact subglacial cones today suggests ongoing volcanic activity (Spiegel et al., 2016). Otherwise, basal friction with the ice sheet would have thoroughly eroded these structures (Van Wyk de Vries, 2018). Additionally, high regional heat fluxes and geomagnetic anomalies in West Antarctica suggest that the rift remains active to the present (Blankenship et al., 1993; Shapiro & Ritzwoller, 2004; Schroeder et al., 2014; Geyer et al., 2023).

The impacts of volcanic processes on the cryosphere and Earth's climate system, including decreased ice albedo (e.g. Bray 1979, Möller et al., 2019) and outgassing of sulfur aerosols and CO_2 (e.g. Handler, 1989; Huybers and Langmuir, 2006; Aubry et al., 2022) have been investigated over a range of timescales. While it is widely understood that nearby volcanic activity can accelerate ice melting, less is known regarding how a shrinking ice load at the surface influences magmatic systems at depth. Several solid Earth phenomena have been proposed to be triggered by deglaciation and to play into complex glacio-volcanic feedback loops: (1) changes in the crustal stress field, (2) a raised geotherm, and (3) a decrease in lithostatic pressure.

Firstly, when an ice load above a magma chamber retreats, time-dependent changes in the crustal stress field occur that affect magma transport through the crust by changing the likelihood of the chamber to rupture and initiate dikes. Flexure of the crust during isostatic rebound creates tensile stresses in the upper crust, promoting dike formation (Mora and Tassara, 2019; Wilson and Russell, 2020). This principle applies regardless of the nature of the load being removed; for example, Satow et al. (2021) suggested that a decrease in sea-level above the crust is capable of triggering dikes from the Santorini magma chamber.

In addition, a shrinking ice load can raise the geotherm, thereby extending the length of the melting column in the mantle and increasing melt flux through decompression melting (Sigmundsson et al., 2010; Van Wyk de Vries, 2018). Jull and Mackenzie (1996) modeled increased melt generation in response to the removal of an axisymmetric ice sheet above a mid-ocean ridge, with application to Iceland. Building on this work, Maclennan et al. (2002) examined this effect regarding volcanism in Iceland following the Last Glacial Maximum; they found that immediately after deglaciation, Icelandic eruption rates were 30–50 times higher than present-day levels and persisted for over 1000 years post-deglaciation, owing to increased melt generation via decompression.

An intuitive consequence of unloading above a crustal magma chamber is the decrease in lithostatic pressure (pressure due to the weight of the overlying material), which affects the thermodynamic state and stability of different magmatic phases at depth. To the authors' knowledge, the effect of such decreasing overburden pressure on internal magma chamber dynamics has yet to be investigated. While past studies proposed a correlation between deglaciation and volcanic activity (Huybers and Langmuir, 2009; Rawson et al., 2016), the physical mechanisms linking dynamic ice loads and the evolution of underlying magmatic systems remain unclear. Consequently, assessments of the stability of the West Antarctic Ice Sheet and projections of its contribution to future sea-level rise lack potentially crucial information. This highlights the need for physics-based modeling of subglacial magma chambers subjected to retreating ice loads to quantify the risk of accelerated melting of the West Antarctic Ice sheet due to ice unloading-triggered volcanism (a step beyond enforcing a boundary condition of high background geothermal heat flux in the proximity of the ice sheet (e.g., Reading et al., 2022).) To address this gap, we simulate the evolution of West Antarctic magma chambers subject to cooling (leading to crystallization and exsolution), viscoelastic stress relaxation, magma recharge, and ice unloading. Specifically, we test different rates of decreasing lithostatic pressure due to a shrinking surface load. Chen et al. (2006) estimate the rate of deglaciation-related surface unloading to be on the order of $10^{-5}\ Pa \cdot s^{-1}$ in West Antarctica based on GRACE satellite data. We consider this a conservative estimate for the modern-day rate of ice unloading in West Antarctica, given the continuous increase in atmospheric CO_2 levels through to the present. We also test rates of ice removal two orders of magnitude higher to anticipate accelerated ice loss in West Antarctica. For context, some ice streams of West Antarctica have experienced rates of ice thinning on the order of $10^{-0.5}\ Pa\ s^{-1}$ in the last decade (Hogg et al., 2021). For simplicity, we assume a linear lithostatic pressure drop over time for the removal of a finite surface load. We apply this forcing to a thermomechanical magma chamber model (Degruyter and Huber 2014; Scholz et al., 2023) parametrized for West Antarctic basalt magmas with mixed CO_2 and H_2O contents to simulate and characterize the response of magma chamber evolution and eruption behavior to ice unloading. This physical model of unloading can be extended to investigate the response of magma chambers to the removal of any other uniform surface load, such as sudden reductions in sea-level over submarine volcanoes and erosion of overlying material during landslides or flank collapse.

2 Methods

To simulate WARS volcanoes, we employ a thermomechanical magma chamber model that includes water and carbon dioxide as magmatic volatile species (Degruyter and Huber, 2014; Scholz et al., 2023), tailored to West Antarctic Rift basalt compositions. Most exposed WARS deposits are part of the Marie Byrd Land (MBL) Province of West Antarctica (LeMasurier, 2013). To develop melting curves and H_2O-CO_2 solubility parametrizations specific to WARS basalts, we utilize whole rock compositions of basalts from MBL from the GEOROC database (https://georoc.eu/.) to compute an average anhydrous magmatic composition (DIGIS Team, 2023). The major oxide contents of the average anhydrous WARS basalt composition used in this study and several parameters for the magma chamber model are provided in Table 1. Sample compositions and locations used to determine the average composition, as well as their associated publications are provided in Table S1.

Table 1. Anhydrous Composition and Model Parameters for WARS Basalt Anhydrous oxide abundances in wt. %, the parameter space covered by the rhyolite-MELTS v.1.1.0 simulations, and the derived parameters for the WARS magma chamber model.

Major Oxide Abundances for Anhydrous Wars Basalt Composition

	SIO_2	**TIO_2**	**AL_2O_3**	**FEO_T**	**MNO**	**MGO**	**CAO**	**NA_2O**	**K_2O**	**P_2O_5**	**TOTAL**
wt. %	46.88	3.29	15.18	12.36	0.19	6.77	10.38	3.12	1.14	0.70	100.0

Parameters for WARS Magma Chamber Model

Symbol	Definition	Value	Units
$\boldsymbol{c_m}$	specific heat capacity of melt	1142	$J\,kg^{-1}\,K^{-1}$
$\boldsymbol{c_x}$	specific heat capacity of crystal	1160	$J\,kg^{-1}\,K^{-1}$
$\boldsymbol{c_{CO_2}}$	specific heat capacity of CO_2 gas	1200	$J\,kg^{-1}\,K^{-1}$
$\boldsymbol{c_{H_2O}}$	specific heat capacity of H_2O vapor	3880	$J\,kg^{-1}\,K^{-1}$
$\boldsymbol{M_{H_2O}}$	molar mass of water	18.02×10^{-3}	$kg\,mol^{-1}$
$\boldsymbol{M_{CO_2}}$	molar mass of CO_2	44.01×10^{-3}	$kg\,mol^{-1}$
$\boldsymbol{L_e}$	latent heat of exsolution	610×10^3	$J\,kg^{-1}$
$\boldsymbol{L_x}$	latent heat of crystallization	470×10^3	$J\,kg^{-1}$
$\Delta\boldsymbol{P_c}$	critical overpressure	20×10^6	Pa
$\boldsymbol{\alpha_r}$	crustal thermal expansion coefficient	10^{-5}	K^{-1}
$\boldsymbol{\alpha_m}$	melt thermal expansion coefficient	10^{-5}	K^{-1}
$\boldsymbol{\alpha_x}$	crystal thermal expansion coefficient	10^{-5}	K^{-1}
$\boldsymbol{\beta_m}$	bulk modulus of melt	1.2×10^{10}	Pa
$\boldsymbol{\beta_x}$	bulk modulus of crystal	10^{10}	Pa
$\boldsymbol{\beta_r}$	bulk modulus of crust	10^{10}	Pa
$\boldsymbol{\kappa}$	thermal diffusivity of crust	10^{-6}	$m^2\,s^{-1}$
$\boldsymbol{\rho_m}$	melt density	2420	$kg\,m^{-3}$
$\boldsymbol{\rho_x}$	crystal density	2900	$kg\,m^{-3}$
$\boldsymbol{\rho_r}$	density of crust	2500	$kg\,m^{-3}$

Parameter Space for rhyolite-MELTS Simulations

Pressure (MPa)	100-400 (intervals of 50 MPa)
wt. % H_2O	0.25-6 (intervals of 0.25 wt. %)
wt. % CO_2	0-1.1 (intervals of 0.1 wt. %)

153

We derive estimates for the range of initial H_2O and CO_2 contents from volatile compositions presented in Oppenheimer et al. (2011), Moussallam et al. (2014), and Lowenstern (2001). Combining these with our anhydrous WARS basalt composition, we simulate thermodynamic closed-system equilibrium crystallization using rhyolite-MELTS (Gualda et al., 2012). While rhyolite-MELTS v.1.1.0 is optimized for silicic systems, it is the only version of MELTS that accounts for both water and carbon dioxide at crustal pressures (Ghiorso and Gualda, 2015). The melt and crystal densities, specific heats, melt compressibility, and latent heat of melting are the average values of each parameter at the median temperature and pressure of each MELTS simulation. After conducting multiple isobaric down-temperature crystallization runs at various pressures, we fit the outputs of the MELTS simulations via quadratic regression to develop mathematical expressions for (i) crystallinity and (ii) CO_2 and H_2O solubilities as functions of temperature, pressure, and bulk volatile contents.

2.1 Melting Curves

We use 2184 isobaric crystallization simulations on rhyolite-MELTS v.1.1.0 with the average WARS basalt composition calculated from normalized anhydrous whole rock compositions over a range of fixed pressures and different initial CO_2 and H_2O conditions, as described in Table 1 (All MELTS calculations conducted at the oxygen fugacity of the NNO buffer.) From the raw MELTS outputs, we calculate volume fractions for melt, crystals/solids, and magmatic volatile phase (MVP). Employing the Matlab curve fitting application (cftool), we determine the most suitable function to describe the crystal volume fraction in the magma with respect to temperature.

Huber et al. (2009) postulated that the melt fraction (f) of magmas can be parametrized as a power law function with an exponent (b) describing the effect of magma composition:

$$f(T) = \left(\frac{T - T_{sol}}{T_{liq} - T_{sol}}\right)^b, \qquad 0 < b < 1 \qquad \text{[Equation 1]}$$

where T_{liq} is the liquidus temperature and T_{sol} is the solidus temperature. Considering mafic magmas, the power-law parametrization suggests an approximately linear melting curve with temperature (b=1). Indeed, a linear fit for the melting curve (nominally the crystal volume fraction ε_x) as a function of temperature is satisfactory for MELTS simulations across a wide range of pressure, temperature, and volatile contents (Figure S1), with an accurate slope over the entire eruptible range (here taken to be $\varepsilon_x < 0.5$) and the liquidus temperature within 5% error of the MELTS data (see Figure S1).

We require a parametrization of the crystal volume fraction as a function of pressure and mass fractions of H_2O and CO_2 in the magma, in addition to temperature. As such, we perform a quadratic regression on the MELTS data to retrieve the following mathematical expressions for ε_x of WARS basalts as a function of temperature, pressure, and the total mass fractions of water and CO_2 in the magma chamber ($M_{H_2O}^{tot}$ and $M_{CO_2}^{tot}$, respectively):

$$\varepsilon_x(T, P, M_{H_2O}^{tot}, M_{CO_2}^{tot}) = A * T + B \qquad \text{[Equation 2]}$$

where both A and B are functions of $P, M_{H_2O}^{tot}$, and $M_{CO_2}^{tot}$. The definitions of A and B as a function of P, $M_{H_2O}^{tot}, M_{CO_2}^{tot}$ obtained from the quadratic regressions are provided in Tables S2 and S3.

2.2 Volatile Solubility

Following the procedure employed for ε_x, we reprocess the MELTS data for CO_2 and H_2O solubility in the magma. Isolating the simulations that reach volatile saturation while the magma is still eruptible ($\varepsilon_x < 0.5$), we use linear regression to fit the mass fraction of dissolved CO_2 and H_2O in the melt as a function of temperature, pressure, and mole fraction of CO_2 in the gas phase, X_{CO_2}. The resulting equation for dissolved H_2O in the melt is given by:

$$M_{H_2O}^{diss} = c_1 + c_2T + c_3X_{CO_2} + c_4P + c_5\left(T * X_{CO_2}\right) + c_6(T * P) + c_7\left(X_{CO_2} * P\right) + c_8T^2 + c_9(X_{CO_2})^2 + c_{10}P^2 \qquad \text{[Equation 3]}$$

with coefficients c_i listed in Table S4.

While the parametrization for H_2O solubility obtained with this procedure is well-tuned to the MELTS data, the same approach could not be used for the CO_2 solubility; we observe unrealistic spikes in CO_2 solubility within MELTS simulations when the first calcium-bearing phase, clinopyroxene, began to crystallize. These spikes likely reflect the increased activity of Ca^{2+}. In rhyolite-MELTS v.1.1.0, CO_2 dissolved in the melt is assumed to be exclusively present as carbonate species, leading to CO_2 activities co-varying with Ca activities. To refrain from fitting spurious CO_2 solubility values during saturation of Ca-phases in MELTS, we instead employ the Liu et al. (2005) CO_2 solubility model for rhyolitic magmas. This model provides a good fit to the MELTS CO_2 solubility data outside of the misleading spikes due to changes in Ca^{2+} activity. Liu et al. (2005) expresses the mass fraction of dissolved CO_2 (in ppm) by:

$$M_{CO_2}^{diss} = \frac{(P * X_{CO_2})(5668 - 55.99P)(1 - X_{CO_2})}{(T + 273.15)} + P * X_{CO_2}\left(0.4133 * \left[P * \left(1 - X_{CO_2}\right)\right]^{0.5}\right) + 2.041 \cdot 10^{-3} * \left[P * \left(1 - X_{CO_2}\right)\right]^{1.5}.$$

[Equation 4]

Given our target composition is basaltic, we test the Liu parametrization extensively with the to check for consistency with the WARS basalt MELTS outputs (see Figures S2-S4). At the pressure-temperature conditions of interest to this study, the parametrizations agree well with the MELTS data (see Table 1 for valid range of conditions).

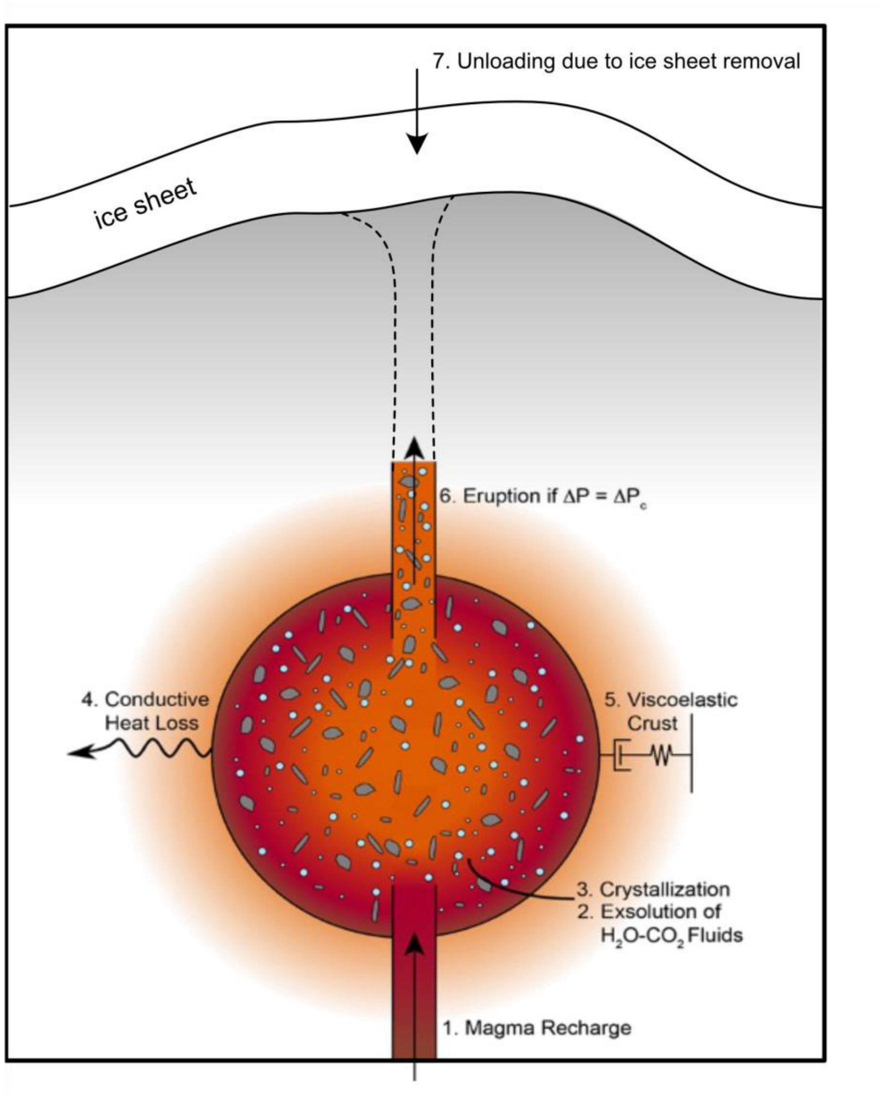

Figure 1. Thermomechanical magma chamber model with simulated ice unloading.

2.3 Magma Chamber Model

We apply our parametrization for WARS basalt crystallization and H_2O and CO_2 solubility to a thermomechanical magma chamber model adapted from Degruyter and Huber (2014) and Scholz et al., 2023. The magma chamber is assumed a spherical body of eruptible magma (less than 50% crystals by volume), surrounded by a viscoelastic shell at depth in the crust, with the magma comprised of a mixture of melt, crystals, and dissolved or exsolved volatiles. Over shorter timescales, the host crust deforms elastically to counteract volume-related pressure changes, while over longer timescales the surrounding crust accommodate overpressure by way of viscous relaxation. Heat loss from the magma chamber occurs through conduction to the surrounding crust, promoting crystallization of melt in the magma chamber and exsolution of H_2O and CO_2 as a magmatic volatile phase (MVP). As magma is injected into the system at a specified recharge rate, the chamber pressurizes and will rupture and trigger an eruption if a critical overpressure ΔP_c is achieved. The magmatic overpressure, ΔP, is defined as the difference between the pressure in the chamber and the lithostatic pressure exerted on the chamber. In times of repose between eruptions, there is no mass outflow. Once the critical overpressure for an eruption is reached, the mass outflow rate is set to $10^4\ kg \cdot s^{-1}$, until pressure returns to lithostatic and mass outflow ceases. Without any unloading, the processes of magmatic injection, cooling, and viscous relaxation compete to control the magma chamber evolution. Degruyter and Huber (2014) define characteristic timescales for these processes; comparing these timescales provides a means to assess the relative efficiency of each process within a simulation of magma chamber evolution.

The timescale of magmatic injection is given by the ratio of the initial mass of the chamber and magmatic recharge rate:

$$\tau_{in} = \frac{\rho_0 V_0}{\dot{M}_{in}} \qquad \text{[Equation 5]}$$

The timescale of cooling is defined as follows:

$$\tau_{cool} = \frac{V_0^{2/3}}{K} \qquad \text{[Equation 6]}$$

where K is the thermal diffusivity of the crust in $m^2\ s^{-1}$.

And lastly, the viscous relaxation timescale, given by:

$$\tau_{relax} = \frac{\eta_{r_0}}{\Delta P_c}. \qquad \text{[Equation 7]}$$

τ_{relax} represents the time delay over which the crust surrounding a magma chamber can, via viscous creep, dissipate a pressure increase equal to that of the critical overpressure required to erupt, ΔP_c. If an overpressure greater than ΔP_c is generated over an interval of time significantly shorter than τ_{relax}, the surrounding crust will respond elastically, unable to dissipate the overpressure, leading to eruptions. As in Degruyter and Huber (2014), the effective viscosity of the crust is a function of the crustal rheology and the temperature distribution around the chamber, which evolves with time. We introduce an additional timescale, τ_{ice} for the rate of lithostatic pressure reduction due to deglaciation at the surface (ice unloading rate), which is described in greater detail in the following section. The governing equations for conservation of total mass, CO_2 and H_2O mass, and enthalpy within the magma chamber model follow the derivations from Scholz et al. (2023), with the WARS basalt parametrizations provided in Tables S2-S4.

2.4 Pressure Unloading from Ice Removal at the Surface

To model ice unloading over a magmatic system, we decompose the primary variable governing magma chamber pressure in the Scholz et al. (2023) model into the sum of the lithostatic pressure (P_{lit}) and the magmatic overpressure (ΔP):

$$P = P_{lit} + \Delta P. \qquad \text{[Equation 8]}$$

Differentiating with respect to time we have:

$$\frac{dP}{dt} = \frac{dP_{lit}}{dt} + \frac{d\Delta P}{dt} \quad . \qquad \text{[Equation 9]}$$

Without any unloading, the lithostatic pressure remains constant over time, and thus the change in absolute pressure in the chamber is equal to the rate of change of magmatic overpressure. To investigate various scenarios of magma chamber evolution across a wide range of initial conditions, we consider different linear rates of lithostatic pressure decrease acting upon a wide range of potential WARS magma chambers (see Tables 4 and 5). To prevent unrealistic lithostatic pressure drops (i.e., unloading after the ice is completely removed), we prescribe a maximum lithostatic pressure drop ($\Delta P_{lit,max}$) which is set to the pressure associated with removing the entire ice sheet. We run additional simulations of unloading associated with the removal of 1.5 km and 2 km thick ice sheets with the same fixed rates of lithostatic pressure decrease for comparison (see Section 3.1).

We define the deglaciation timescale (τ_{ice}) mentioned above as the duration for removing an ice sheet of specified thickness from atop the magma chamber, given a specific rate of unloading ($\frac{dP_{lit}}{dt}$):

$$\tau_{ice} = \left|\Delta P_{lit,max}\left(\frac{dP_{lit}}{dt}\right)^{-1}\right|. \quad \text{[Equation 10]}$$

If the magma is still eruptible beyond τ_{ice} ($\varepsilon_x < 0.5$), the lithostatic pressure remains constant at $P_{lit}(t = 0) - \left|\Delta P_{lit,max}\right|$ for the remainder of the simulation. Regardless of whether the chamber is erupting or in repose, we solve for the pressure, temperature, crystal volume fraction, and other dynamic quantities while the chamber is subjected to magmatic recharge and heat loss to the surrounding crust.

Although this model is simple, its capacity to simulate nonlinear behavior enables the mapping of the magma chamber response to unloading-induced perturbations across an extensive parameter space. We generate an ensemble of 3888 simulations from our parametrized magma chamber evolution model, exploring various initial magma chamber volumes, depths within the crust, magmatic recharge rates, initial H_2O and CO_2 contents, and rates of lithostatic pressure unloading (Table 2). The ice unloading rates considered in this paper, $10^{-5}\ Pa \cdot s^{-1}, 10^{-4}\ Pa \cdot s^{-1}$, and $10^{-3}\ Pa \cdot s^{-1}$, correspond to the removal of a 1-km ice load over a period of approximately 30,000 years, 3000 years, and 300 years, respectively.

Table 2. Thermomechanical Magma Chamber Model Simulations

Model Inputs

Initial Volume (km^3)	$0.5\ km^3 - 10\ km^3$ in intervals of ~1 km^3
Depth (km)	$6\ km - 10\ km$ in intervals of 2 km
Magma Recharge Rate ($kg \cdot s^{-1}$)	$10\ kg \cdot s^{-1} - 100\ kg \cdot s^{-1}$ in intervals of ~5 $kg \cdot s^{-1}$
Initial wt. % H_2O	$1\ wt.\% - 2\ wt.\%$ in intervals of 0.5 $wt.\%$
Initial wt. % CO_2	$0.05\ wt.\% - 0.5\ wt.\%$ in intervals of ~0.025 $wt.\%$
Rate of Unloading ($Pa \cdot s^{-1}$)	$0\ Pa \cdot s^{-1}$ $10^{-5}\ Pa \cdot s^{-1}$ $10^{-4}\ Pa \cdot s^{-1}$ $10^{-3}\ Pa \cdot s^{-1}$

Rate vs. Timescale of Unloading: 1-km Ice Sheet

Rate of Unloading ($Pa \cdot s^{-1}$)	Time Required to Remove 1-km Ice Sheet (years)
$\mathbf{10^{-5}\ Pa \cdot s^{-1}}$	30,000
$\mathbf{10^{-4}\ Pa \cdot s^{-1}}$	3000
$\mathbf{10^{-3}\ Pa \cdot s^{-1}}$	300

297

3 Results

3.1 A Critical Rate of Ice Unloading

Ice unloading begins to dramatically affect magma chamber behavior when the ice unloading timescale approaches that of the other processes impacting magma chamber evolution (i.e., magmatic recharge, cooling, and viscous relaxation). At such conditions, the reduced confining pressure associated with unloading allows the magma to expand volumetrically generating overpressure. This source of overpressure associated with unloading acts in opposition to the prescribed lithostatic pressure decrease. As described in Section 2.3, within the model, eruptions occur when the difference between the magma chamber pressure and the lithostatic pressure at a given time exceeds the critical overpressure, ΔP_c. As lithostatic pressure decreases over time, the absolute pressure threshold required to reach ΔP_c is lowered. In some cases, this enables additional eruptions to occur, solely due to unloading.

Figure 2 demonstrates one such situation, where a volatile-undersaturated magma chamber is pushed to erupt an additional time when forced with a sufficient unloading rate. With the intermediate and high unloading rates (i.e., removing an ice sheet of 1 km thickness over approximately 3000 and 300 years, respectively), the magma chamber reaches the critical overpressure earlier, producing an additional eruption that evacuates an additional $5 \times$

10^7 metric tons ($5 \times 10^{10}\ kg$). This additional erupted mass due to the ice unloading is an order of magnitude greater than, for example, the lava flows erupted from the summit of Mt Etna on July 31, 2021 (INGV, Rep. N 31/2021, ETNA). Such a rate-dependent increase in eruptions during the duration over which unloading is active also occurs in simulations of magma

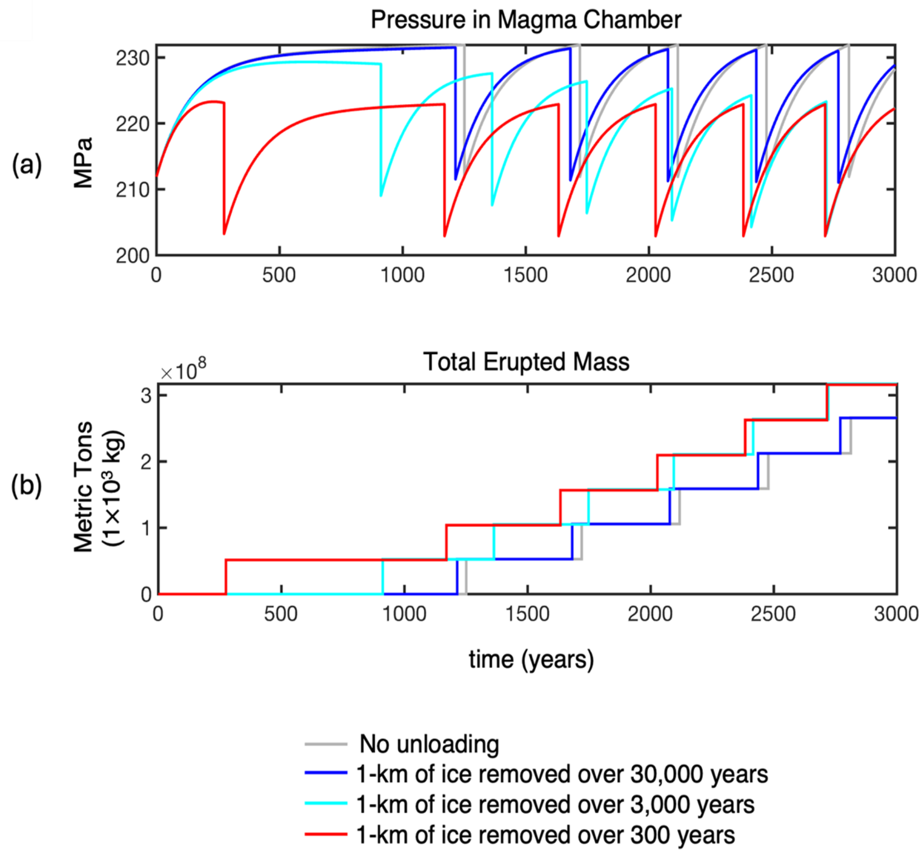

Figure 2. Increase in Total Erupted Mass with Unloading Rate: Volatile-Undersaturated Timeseries of pressure and cumulative erupted mass over 3000 years of magmatic evolution for an 8-km deep magma chamber initially with a volume of 5 km^3, 2 wt. % H_2O, and 500 ppm CO_2, subjected to a constant magmatic recharge rate of $20\ kg \cdot s^{-1}$. The chamber remains volatile-undersaturated during this time interval. Vertical drops in pressure correspond to eruption events. The slowest unloading scenario (blue) plots closely over the zero-unloading case (gray). In the first 1000 years, the slow unloading case is unable to reach the critical overpressure threshold, however, the overpressure generated through unloading causes the magma chamber to pressurize and erupt earlier than it would without unloading. In the first 1000 years of the intermediate- (cyan) and fast- unloading scenarios (red), the combined overpressure from magmatic recharge and unloading surpasses the critical overpressure and triggers an additional eruption.

chambers at saturation conditions, despite the ability for the exsolved volatiles to buffer overpressure (see Fig. S5).

We compare the sensitivity of the magma chamber response to both the rate of ice unloading and the total thickness of ice removed in Figure 3. While the integrated lithostatic pressure change is small in comparison to crustal pressures, a sufficient rate of unloading for a constant amount of ice removed (e.g., 1 km of ice load shaved off) can modulate the eruptive behavior. For both the lowest and intermediate unloading rates (blue and cyan, respectively) in Figure 3, the pressure trends are indistinguishable regardless of whether the ice removed is 1 km, 1.5 km, or 2 km thick. Only in the case of the highest unloading rate (red; Figure 3c and f) does the

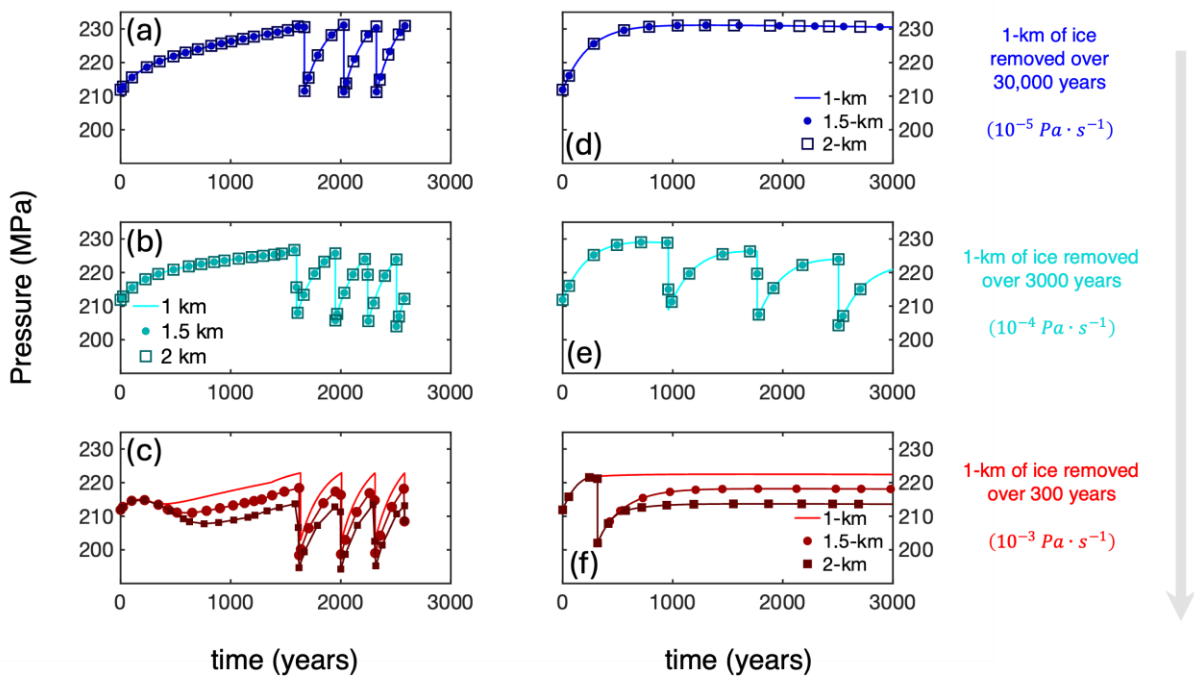

Figure 3. Unloading Rate vs. Magnitude (a)-(c) Pressure timeseries for an 8-km deep magma chamber with initial conditions of 1.25 km^3 volume, 2 wt. % H_2O, and 500 ppm CO_2, subjected to a constant magmatic recharge rate of 6 $kg \cdot s^{-1}$ and (a) slow, (b) intermediate, and (c) fast unloading scenarios. For a given rate of unloading in each panel, the pressure evolution is shown for three scenarios involving different magnitudes of unloading (1 km, 1.5 km, and 2 km of ice removal). (d-f) Pressure timeseries for an 8-km deep magma chamber with initial volume of 7 km^3 and volatile contents of 1 wt. % H_2O and 5000 ppm CO_2, subjected to a constant magmatic recharge rate of 30 $kg \cdot s^{-1}$ and the same unloading rates.

magnitude of ice removal cause subtle deviations.

For the smaller chamber in Figure 3 (panels a-c), the chamber cools efficiently ($\tau_{cool} = 1.4 \times 10^4$ years, $\tau_{\mathrm{in}} = 1.6 \times 10^4$ years, $\tau_{\mathrm{relax}} = 3.2 \times 10^4$, years), rheologically locking the magma via crystallization. Consequently, the total number of eruptions and erupted mass are identical regardless of the magnitude of ice removed. There are eruptions from the magma chamber in Figure 3a-c, but these are triggered by second boiling, and hence occur even in the absence of unloading. A bigger magma chamber at the same depth, subjected to a higher rate of magmatic recharge (Figure 3d-f), cools more slowly, maintaining the magma at less than 50 % crystals by volume for longer. The magma chamber from Figure 3d-f does not erupt without unloading, however, forcing with the intermediate unloading rate ($-1 \times 10^{-4}\ Pa \cdot s^{-1}$) triggers several eruption events (Figure 3e; Figure 4). In the case of the highest unloading rate ($-1 \times 10^{-5}\ Pa \cdot s^{-1}$; Figure 3f), a duration of unloading of 300 years is insufficient to counterbalance the dissipation of overpressure via viscous relaxation of the surrounding crust, prior to complete removal of the ice load. If we consider the fast-unloading scenario again in Figure 3f, but increase the thickness of the ice removed, naturally, the magma 'feels' the effects of decompression-induced volumetric expansion for longer. This, coupled with a slower cooling rate (compared to the magma chamber in 3a-c) and reduced pressure required to trigger an eruption enables a single eruption to occur. Figure 4 explores, in isolation, the 1 km ice removal scenarios for the magma chamber in Figure 3d-f, demonstrating that even with the removal of modest amounts of ice (equivalent to less than 5-10% of the lithostatic pressure exerted on a magma chamber at several kilometers deep in the crust), if the rate of ice unloading for a given ice load is sufficient, there are notable differences eruptive behavior. From these observations, we conclude that the rate of unloading plays a greater role in controlling magma chamber evolution than the magnitude of unloading, when considering the removal of km-thick ice loads. Hence, we primarily focus on the effects of unloading rates in Section 4.

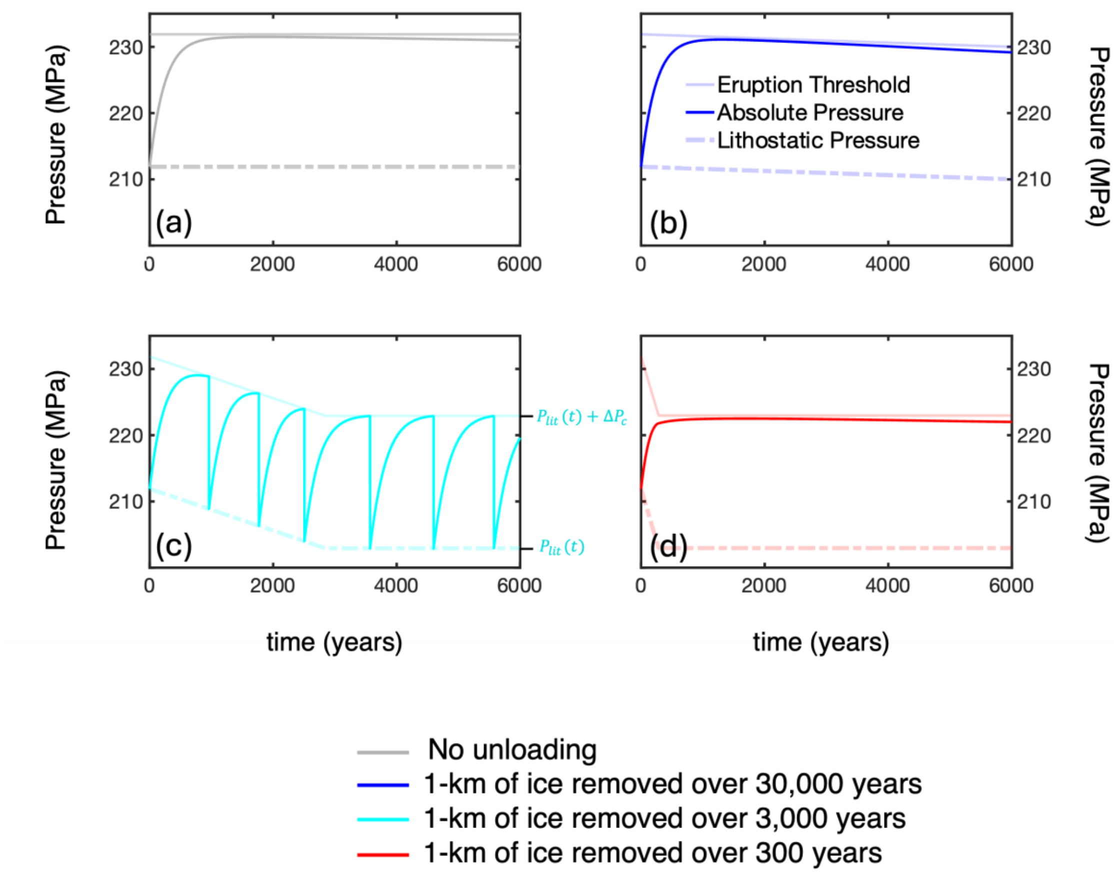

Figure 4. Pressure Budget for Eruption Pressure timeseries for the same magma chamber in Figure 3(d)-(f) subjected to (a) no ice unloading, and 1 km of ice removal at (b) low, (c) intermediate, and (d) high unloading rates, respectively. In (a), (b), and (d) the magma pressure falls just short of the critical overpressure required for eruptions. The highest unloading rate (d) experiences complete removal of the ice load early on, ceasing of active unloading before the critical overpressure is reached. In the intermediate unloading scenario (c), the magma chamber erupts several times, as unloading is active long enough for the lithostatic pressure to drop such that the overpressure reaches the requirement for eruptions.

3.2 Ice Unloading Expedites Exsolution of Magmatic Volatile Phase

Besides the potential for additional eruptions triggered by unloading-induced overpressure, unloading can also expedite or trigger the exsolution of volatiles from magmas on the cusp of volatile saturation. Partitioning of the CO_2 and H_2O between melt and gas bubbles controls magma compressibility and thus the frequency and size of eruptions (Huppert and Woods, 2002; Degruyter et al., 2017; Townsend et al., 2019). All other factors being equal, we find that for magma chambers that are initially volatile-undersaturated, the time to the first exsolution of volatiles decreases by tens to hundreds of years as the rate of ice unloading increases (Figure 5; Figure S6). In Figure 5, while the variations in the total number of eruptions across various unloading rates are subtle, the cumulative mass erupted from the magma chamber is significantly affected by the proportion of eruptions that occur after volatile exsolution, due to increased magma compressibility. As illustrated by Figure 5b-c, the drop in lithostatic pressure also leads to a larger background exsolved gas volume fraction. Even small increases in the exsolved gas volume fraction enhance magma compressibility, augmenting the size of eruptions. The effects of unloading on magmatic volatile phases (and hence the total mass erupted from the system) across the wider parameter space of potential WARS magma chambers are discussed further in Section 4.1.

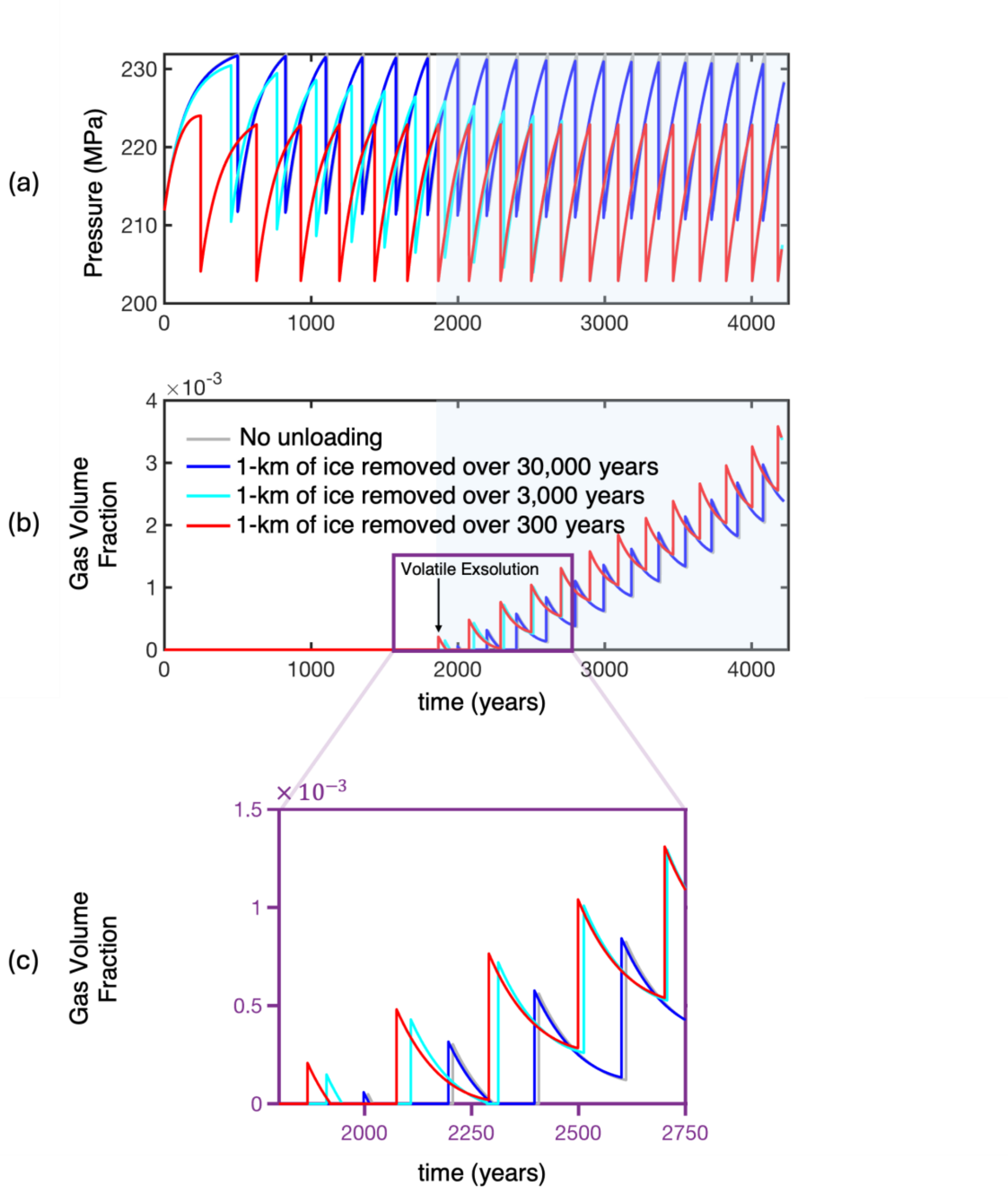

Figure 5. Expedited Onset of Volatile Exsolution Pressure and gas volume fraction timeseries for a magma chamber with a volume of 10 km^3, 2 wt. % H_2O, and 500 ppm CO_2 initially, at depth of 8 km with a constant recharge rate of 12 $kg \cdot s^{-1}$. The magma chamber undergoes two oscillations of volatile saturation, as the pressure buildup toward eruption forces the volatiles to be redissolved in the melt. The pressure drop during an eruption releases the volatiles from solution. As cooling proceeds, the magma chamber becomes for the remainder of the eruptible lifetime of the chamber.

372

4 Discussion

Sections 2.3 and 2.4 introduce representative timescales for the fundamental processes (cooling magmatic injection, viscoelastic relaxation of stresses by the surrounding crust, and ice unloading) competing to determine the evolution of a given magma chamber ($\tau_{cool}, \tau_{in}, \tau_{relax},$ and τ_{ice}, respectively). The ratio of these timescales offers a relative measure of the dominant processes. For instance, if the timescale for magma recharge is significantly smaller than the cooling and viscous relaxation timescales, magmatic recharge can significantly counteract cooling and prolong the duration over which the magma is eruptible. In such a situation, overpressure cannot be efficiently dissipated by viscous creep in the surrounding crust. It is therefore useful to consider the ratios of $\tau_{cool}, \tau_{relax}$, and τ_{ice} and the timescale of magmatic injection, τ_{in}, to obtain the following dimensionless numbers, derived in Degruyter and Huber (2014):

$$\theta_1 = \frac{\tau_{cool}}{\tau_{in}}, \qquad \theta_2 = \frac{\tau_{relax}}{\tau_{in}}, \qquad \theta_3 = \frac{\tau_{ice}}{\tau_{in}} \qquad \text{[Equations 11-13]}$$

The timescale of ice unloading (Equation 10) is a function of the total magnitude of lithostatic pressure removed atop the system and the rate at which the lithostatic pressure decreases from ice unloading. Degruyter and Huber (2014) established a dimensionless eruption regime diagram using θ_1 and θ_2. We visualize our magma chamber parameter space as a 3D extension of their scaling relationships, with $\theta_1 = \frac{\tau_{cool}}{\tau_{in}}$ and $\theta_2 = \frac{\tau_{relax}}{\tau_{in}}$on the x- and y- axes respectively and $\theta_3 = \frac{\tau_{ice}}{\tau_{inj}}$ plotted along the axis extending into and out of the plane of the page (Figure 6a). In the following subsections we use this dimensionless 3D space to discuss the regimes of magma chambers most vulnerable to perturbations in cumulative erupted mass (and thus enthalpy released to the ice sheet). Subsequently, we place these findings in the context of post-Last Glacial Maximum trends in volcanism in the Andes and address future implications of the ice-volcanism feedback loop.

4.1 Unloading Effects on Total Erupted Mass

Within the context of the dimensionless timescale ratios (Equations 11-13), our results highlight the combinations of magma chamber conditions that are sensitive to unloading-induced perturbations in total erupted mass. Figures 6b-d plot the percent increase in the total mass erupted with ice unloading, as compared to the equivalent magma chamber simulation without unloading. Significant unloading-induced perturbations in the total erupted mass from a magma chamber occur when both the cooling timescale and the viscous relaxation timescales are comparable or greater than the magma recharge timescale (θ_1, θ_2>1). Within this range of magma chamber conditions, ice unloading raises the total erupted mass even at the most conservative unloading rate ($1 \times 10^{-5}\ Pa \cdot s^{-1}$). Deeper in the crust, the viscous relaxation of accumulated stresses inside the magma chamber by the surrounding crust dominates magma chamber evolution, reducing the ability for the magma chamber overpressure to exceed the eruption threshold. At shallower depths (larger values of θ_2), where magma chambers cool more rapidly and are generally more short-lived, there is a clear trend of increasing cumulative mass erupted with increased unloading rate. In addition, the unloading effects can outcompete that of higher rates of magmatic injection, extending the region of sensitivity to increases in erupted mass. Exceedingly rapid magmatic recharge will overprint the effects of unloading unless unloading occurs at a critical rate (i.e. the unloading timescale is less than or on the order of the magmatic injection timescale, $\theta_3 \leq 1$.)

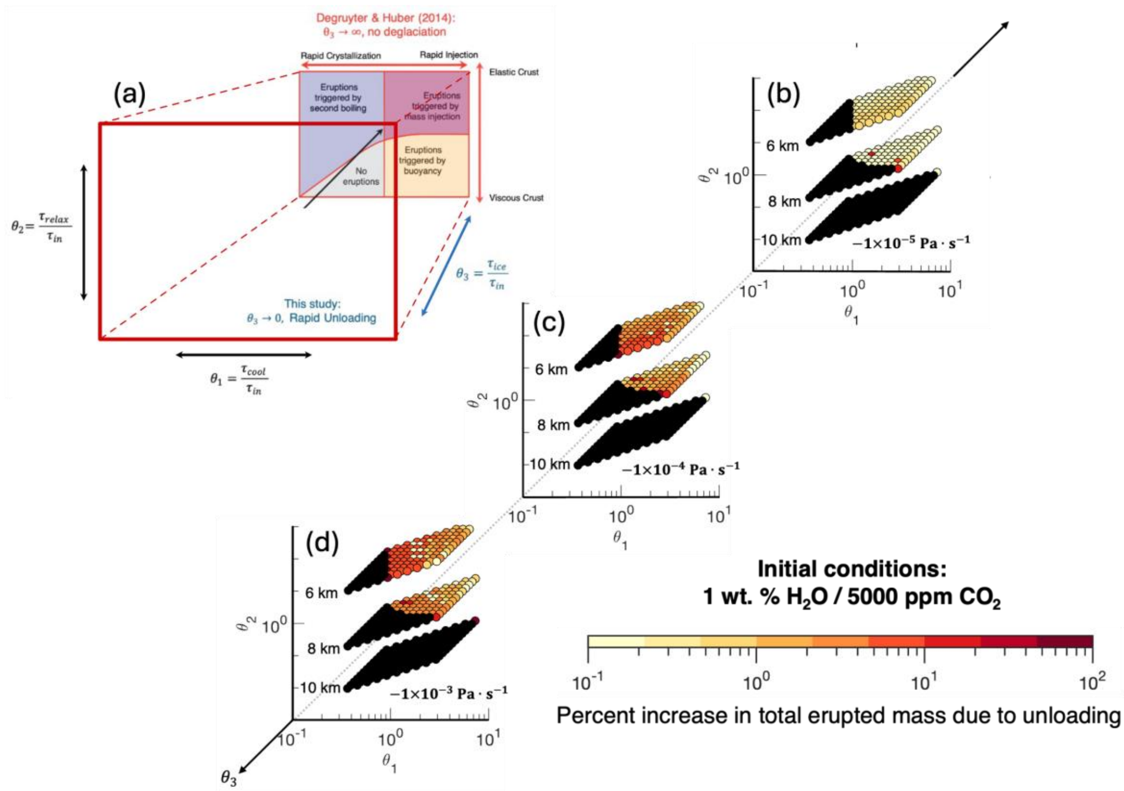

Figure 6. Increase in Mass Erupted with Unloading (a) Modified regime diagram from Degruyter and Huber (2014). (b)-(d) plot the percent change in the total erupted mass between the zero-unloading case and all non-zero unloading scenarios for magma chambers with 1 wt. % H_2O and 5000 ppm CO_2 initially. Black circles represent magma chambers that do not in either case.

As already described in Section 3.1, the unloading-related increase in erupted mass illustrated by Figure 6 is in part driven by additional unloading-triggered eruption events. These eruptions are driven by two underlying mechanisms; firstly, overpressure is generated through the decompression-induced volumetric expansion of the magma. Secondly, unloading alters the pressure budget required for the magma chamber to erupt, and as the overburden pressure decreases, a lower absolute pressure in the magma chamber is required to exceed the overpressure criteria for eruptions (Equation 8; Figure 4). These combined effects result in eruptions that would not occur in the absence of unloading, leading to a greater cumulative mass erupted over the lifetime of the magma chamber. As demonstrated in Figures 3 and S5, these additional unloading-triggered eruptions are observed from magma chambers that are volatile-undersaturated and oversaturated alike. For magma chambers initially below the threshold of volatile saturation, these eruptions tend to occur while the volatiles are completely dissolved in the melt, since the magma is less compressible without exsolved gas bubbles (see Figure S9).

An additional source of the observed increase in cumulative erupted mass with unloading rate (Figure 6) is the quantity of larger-sized eruptions, resulting from increased magma compressibility, as decompression promotes the release of volatiles from the melt. In Section 3.2, we show that with sufficient unloading rates, magma chambers initially below saturation conditions begin to exsolve volatiles earlier, due to decompression. A regime diagram demonstrating the extent of sensitivity of initially volatile-undersaturated magma chambers to an expedited transition to volatile saturation is provided in Figure S10. Interestingly, the magma chambers that are most sensitive to earlier volatile saturation with unloading are cases that fail to erupt, due to insufficient magmatic recharge (compare Figures 6 and S10); these magma chambers are just short of the requirements to erupt, but with slight perturbations in magmatic recharge could be pushed beyond the threshold. Magma chambers subjected to unloading will experience volatile saturation significantly earlier in their evolution, resulting in the potential for more eruptions while the magma is volatile-saturated (and hence more large eruption events). Nevertheless, there is still modest sensitivity to an earlier onset of volatile saturation with sufficient rates of unloading for magma chambers that do erupt, resulting in a greater cumulative mass erupted even without a change in the total number of eruptions (Figure 7). Regardless of whether the chamber is initially volatile-saturated or becomes saturated later, with ice unloading (even if only active for a short duration with respect to the eruptible lifetime of the magma chamber), the volatile solubility is permanently reduced, resulting in increased magma compressibility and larger eruptions. Such long-term effects, where even for short durations of ice removal (~300 years), the removal of 1 km of ice results in an increased cumulative erupted mass long after the ice load is completely gone, are the most consequential in terms of the broader climate implications. Essentially, even if modern anthropogenic warming were curtailed immediately, the unloading that WARS subglacial volcanoes already experienced will still affect their behavior for hundreds to thousands of years to follow.

Given these unloading effects on the total mass erupted, we observe a stronger sensitivity of magma chambers that are initially saturated (i.e., Figure 6b-d) subject to unloading compared to that of magma chambers that are initially volatile-undersaturated (compare with Figure S7). While the magma chamber is volatile-saturated and thus more compressible, a larger amount of mass must be evacuated in a single eruption to restore the magma chamber pressure to lithostatic (consider the effect of these larger eruptions compounded over the entirety of the eruptible lifetime of an initially volatile-saturated magma chamber, as compared to that for a magma chamber that only becomes saturated later in its evolution.)

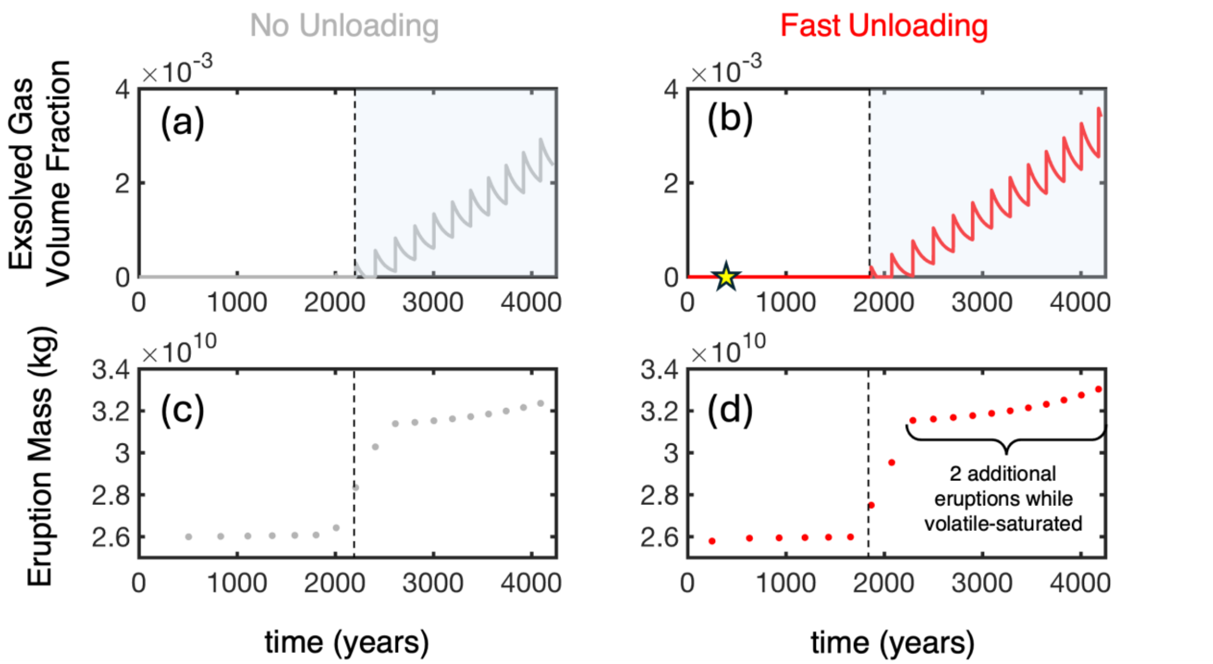

Figure 7. Eruptions Before and After Volatile Exsolution Revisiting the magma chamber evolution from Figure 5, where the onset of volatile exsolution is expedited by 150 years the highest unloading rate for the removal of 1-km of ice ($-1 \times 10^{-4}\ Pa \cdot s^{-1}$). At this rate, the ice load is completely removed by 300 years (indicated by yellow star). Eruptions that occur while H_2O and CO_2 are still dissolved in the melt are significantly smaller than those post volatile exsolution because of the profound increase in magma compressibility with subtle increases in the exsolved gas volume fraction. When the magma chamber is subjected to the fast-unloading scenario, it erupts two additional times while the chamber is volatile-saturated than the equivalent magma chamber without unloading.

4.2 Addition to Enthalpy Budget: Consequences for Deglaciation in West Antarctica

An increase in mass erupted from a subglacial magma chamber means more heat is introduced to the ice sheet. The enthalpy of an eruption is calculated as the sum of the sensible heat from the erupted material, $Q_{sensible}$, and the latent heat of crystallization and volatile exsolution, $Q_{Latent,x}$ and $Q_{Latent,e}$ respectively:

$$H_{erupt} = Q_{sensible} + Q_{Latent,x} + Q_{Latent,e}, \quad \text{[Equation 14]}$$

where

$$Q_{sensible} = \rho c T_{er} V_{erupt}, \quad \text{[Equation 15]}$$

$$Q_{Latent,x} = \rho_x \varepsilon_x V_{erupt} L_x, \quad \text{[Equation 16]}$$

and

$$Q_{Latent,e} = \rho_g \varepsilon_g V_{erupt} L_e. \quad \text{[Equation 17]}$$

L_x and L_e are provided in Table 1. Here, T_{er}, ε_x, and ε_g are the temperature, volume fraction of crystals, and gas volume fraction, respectively, inside the magma chamber at the midpoint of the eruption. A regime diagram plotting the total deviation in total erupted enthalpy from magma chambers given various rates of unloading is provided in Figure S8.

Unloading-triggered volcanism will transfer additional enthalpy directly to the ice sheet base and/or surface, once the erupted material penetrates through the ice. We can consider a theoretical average additional heat supply to the ice due to the volcanic response to unloading over time as follows:

$$q = \frac{H_{erupt}^{with\ unloading} - H_{erupt}^{without\ unloading}}{eruptible\ lifetime\ of\ magma\ chamber} \quad \text{[Equation 19]}$$

where the eruptible lifetime of the magma chamber is the duration of time over which the magma remains below $\varepsilon_x = 0.5$. Figure 8 demonstrates this additional heat input to the ice sheet for many magma chambers with initial volatile contents of 1 wt. % H_2O and 5000 ppm CO_2 (volatile-saturated throughout their entire evolution). While an additional heat released over time due to unloading could result from a larger amount of erupted mass from the magma chamber in the absence of significant deviations in the eruptible lifetime of the magma chamber, or the same (or less) erupted mass in total over a condensed eruption timeline, we find that the deviation in the eruptible lifetime of the magma chamber due to unloading is negligible for magma chambers that are initially volatile-saturated (See Fig. S11). Hence, the sensitivity of magma chambers to this additional source of heat released over time in Figure 8 is primarily due to the increase in the total mass erupted with unloading. The highest rates of additional heat released due to unloading in Figure 8 are exhibited from magma chamber simulations subject to the intermediate unloading rate ($-1 \times 10^{-4}\ Pa \cdot s^{-1}$, equivalent to removing 1 km of ice thickness over 3000 years). At even higher unloading rates, the 1-km ice load is removed rapidly with respect to the eruptible duration of the magma chamber simulation; once unloading 'shuts off' the volumetric expansion-driven overpressure is gone and only the unloading effects of greater magma compressibility and reduced pressure threshold for eruptions can increase the cumulative mass erupted in the longer term. For magma chambers subject to less extreme rates of unloading, all effects are in operation for a larger fraction of the magma chamber longevity, allowing for the cumulative heat released due to unloading-triggered eruptions and eruptions of larger sizes to compound over time. It is important to note that while modern day ice loss rates in West Antarctica may be quite rapid, the subglacial magma chambers of the WARS have been experiencing ice unloading over longer timescales since the last ice age.

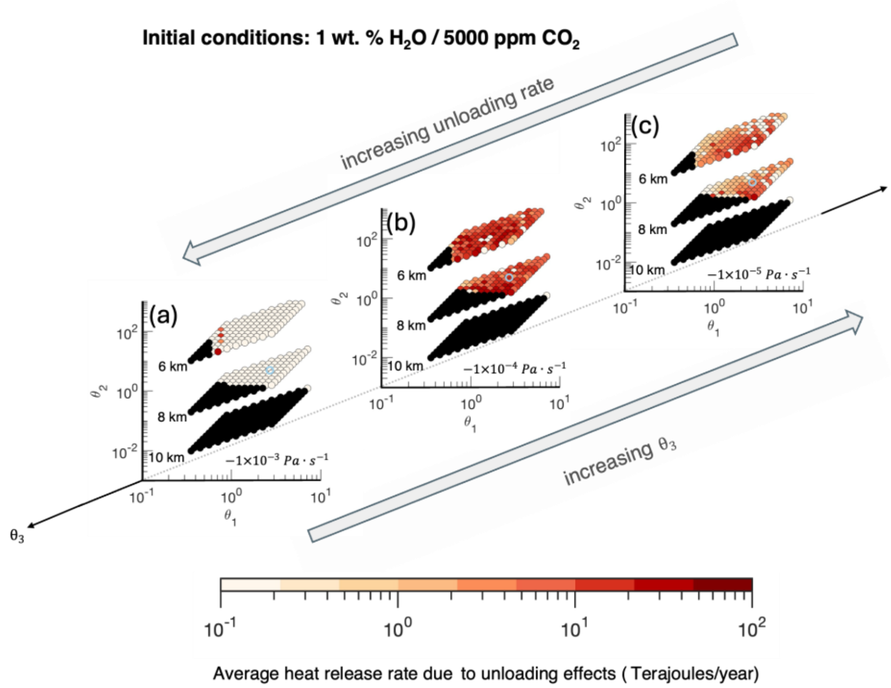

Figure 8 Regime diagram for magma chamber simulations at depths 6, 8, and 10 km in the crust, indicating the additional heat released in Terajoules per year due to unloading at various rates. All magma chambers have initial volatile contents of 1 wt. % H_2O and 5000 ppm CO_2). The magma chamber circled in light blue is discussed further in the text.

To illustrate the risks associated with failing to account for the additional supplied from unloading-triggered volcanism in projections of WAIS stability, we consider the magma chamber circled in blue in Figure 8, which releases an additional 10 Terajoules per year at the intermediate unloading rate ($10^{-4}\ Pa \cdot s^{-1}$). We calculate the amount of ice that can be melted by an additional 10 Terajoules ($1 \times 10^{12}\ J$) per year to the ice sheet; the heat required to melt a mass, m, of ice is given by:

$$Q = m \cdot \Delta H_f \qquad \text{[Equation 20]}$$

Taking the heat of fusion of water, ΔH_f, to be 334 J/g, the heat from unloading-triggered volcanism is capable of melting ~ 3×10^9 kg of ice per year, or equivalently ~3×10^6 m^3 of ice per year. This estimate stands for a single subglacial volcano at a depth of 8 km, with an initial volume of 1.5 km^3, subjected to the intermediate rate of unloading (equivalent to the removal of

1 km-thickness of ice over 3000 years). Considering the over 100 potentially active subglacial volcanoes of West Antarctica (Van Wyk de Vries 2018; Geyer et al., 2023), the aggregate may significantly affect the mass balance of the ice sheet. If the erupted material does not penetrate through the ice cover, melted ice can lubricate the base of the ice sheet, facilitating sliding and ice loss to the ocean. Given the vulnerability of the West Antarctic Ice Sheet, this potentially unaccounted heat source warrants consideration in projections of ice loss from West Antarctica.

4.3 Supporting Evidence from the Geologic Record

While the need to understand consequences of glacio-volcanic feedbacks primarily concerns volcanism beneath the West Antarctic Ice Sheet today, it is difficult to probe recent subglacial volcanic activity (Iverson et al., 2017). Perhaps the most complete coupled records of volcanism and deglaciation are from the Southern Volcanic Zone of the Andes in South America, where the Patagonian ice sheet grew to its greatest thickness of 1600 m or more on the shoulders of several composites between about 35 and 18 ka, and retreated very rapidly between 18 and 15 ka (Singer et al., 2008; Watt et al., 2013; Rawson et al., 2016; Mixon et al., 2021, Moreno Yaeger et al., 2022, and in review).

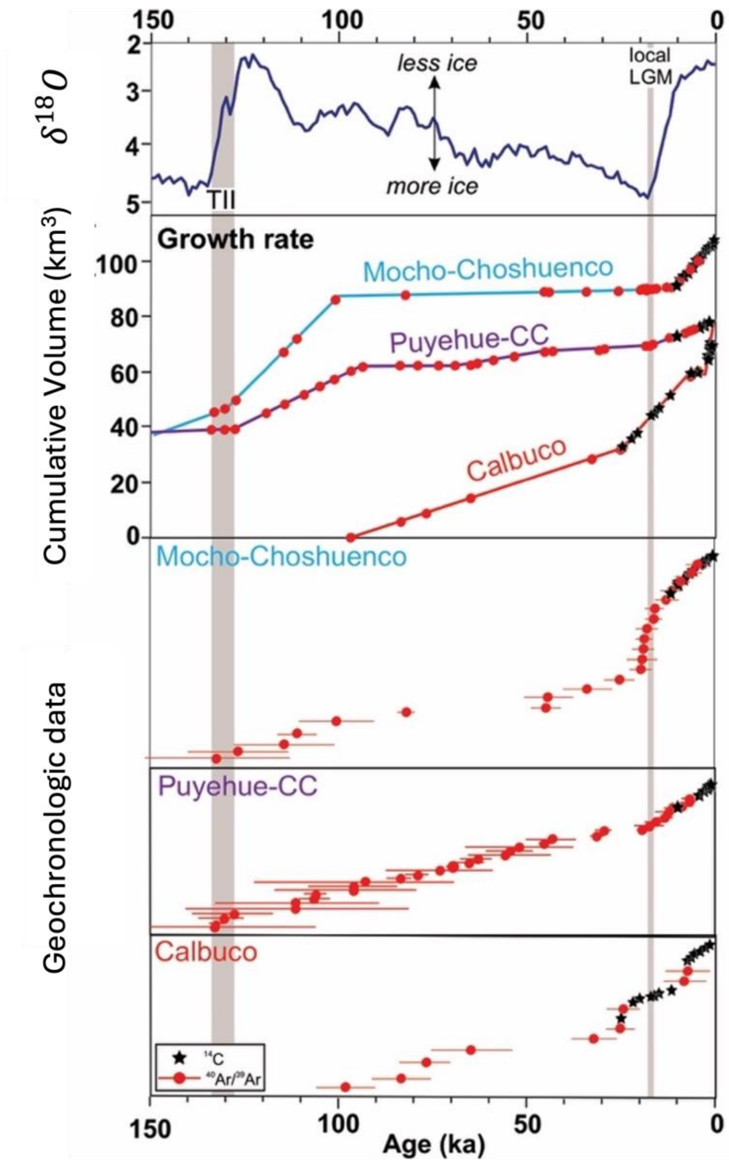

Figure 9. Records of cumulative volume erupted over time from three composite arc front volcanoes in the Andean Southern Volcanic Zone. $^{40}Ar/^{39}Ar$ ages from effusive lava flows and ^{14}C ages for tephra deposits have been used together with field relations to estimate eruptive volumes and growth rates (data from Singer et al., 2008; Mixon et al., 2021; Moreno Yaeger et al., 2023 and in review). Comparison with the global marine proxy record for global ice volume (Lisiecki and Raymo, 2005) indicates that following both Termination II (TII) and the local Last Glacial Maximum (LGM), cone growth rates increase significantly.

Figure 9 illustrates the increase in both cumulative volume erupted and the number of eruptions observed in the records from Calbuco, Mocho-Choshuenco and Puyehue-Cordon Caulle volcanoes in the Andean arc following the local Last Glacial Maximum at 18 ka. These reconstructions that span the rapid, <3 kyr, transition from glacial to post-glacial conditions suggest that there is a link between the rapid unloading of ice from the landscape and upticks in the frequency and volume of eruptions. As we have shown, magma chambers release more mass and heat with sufficiently high rates of ice unloading. Given that erupted volume is proportional to mass erupted, the records from these Andean volcanoes may be an illustration of the unloading-triggered feedbacks outlined in this study. Since the Andean records reflect arc magmas, which typically have higher initial volatile contents than rift magmas, they were likely volatile-saturated during the deglaciation. Our results suggest that volatile-saturated magma chambers are more sensitive to unloading-induced perturbations in erupted mass than magma chambers with a delayed onset of volatile exsolution, and hence the response of Andean volcanoes could be magnified in comparison to volcanoes in rift settings like West Antarctica. The feedbacks of unloading on magma chamber evolution could have accelerated deglaciation in the Andes from the heat released via eruptions and a decrease in ice albedo from subaerial volcanic deposits, potentially amplifying the volcanic response, in turn. Future efforts that couple subglacial volcanic activity with the pace of deglaciation can better account for the instability of the closed feedback loop and hence the risk of runaway ice retreat.

5 Conclusions

We model the evolution of a subglacial magma chamber under various ice unloading rates to understand physical mechanisms linking deglaciation and volcanism, with special consideration of the West Antarctic Rift System. To develop physical intuition for these processes, we consider ice unloading for a wide range of potential magma chambers. We find that a critical rate of unloading increases the total erupted mass from WARS-type subglacial magma chambers, when simulating the removal of realistic ice loads (e.g., thickness on the km-scale). When the rate of ice unloading can compete with the rates of other processes affecting the internal dynamics of the magma chamber (i.e., magmatic recharge, cooling, and viscous relaxation of the surrounding crust), magma chambers produce additional eruptions due to the volumetric expansion of compressible magma inside the chamber, as well as a lowered critical pressure threshold required to trigger eruptions. Additionally, as the rate of unloading increases over magma chambers on the cusp of volatile saturation, the onset of the first exsolution of gas bubbles is expedited significantly. Even after volatile saturation is reached, continued unloading increases the volume fraction of bubbles and hence the compressibility of the magma. The consequence of this increased magma compressibility is that a larger amount of mass must be withdrawn during an eruption to relax the overpressure (Huppert and Woods, 2002; Townsend et al., 2019). Even long after ice unloading ceases, the compressibility of the magma remains permanently elevated due to the reduction in lithostatic pressure, resulting in larger eruptions in the long-term trajectory of the magma chamber. The additional heat associated with such unloading-triggered eruptions is currently unaccounted for in models of the West Antarctic Ice Sheet, despite its potential to perturb the surface mass balance and/or basal sliding rate of such a vulnerable ice sheet. Understanding the role of subglacial volcanism within the closed feedback loop of ice unloading will help reassess West Antarctic Ice Sheet stability.

Acknowledgments

The authors declare no competing interests. Supplementary Information is available for this paper. Correspondence and requests for materials should be addressed to Allie N. Coonin.

This work was supported by NSF- 2121655.

Open Research

The Matlab scripts to run this model are available via Zenodo: https://doi.org/10.5281/zenodo.12188625 (Coonin et al., 2024)

References

1. Aubry, T.J., Farquharson, J.I., Rowell, C.R. *et al.* Impact of climate change on volcanic processes: current understanding and future challenges. *Bull Volcanol* 84, 58 (2022). https://doi.org/10.1007/s00445-022-01562-8
2. Barletta, V.R. *et al.*, Observed rapid bedrock uplift in Amundsen Sea Embayment promotes ice-sheet stability. *Science***360**,1335-1339(2018). DOI:10.1126/science.aao1447
3. Behrendt, J. C., Blankenship, D. D., Morse, D. L., Finn, C. A., & Bell, R. E. (2002). Subglacial volcanic features beneath the West Antarctic Ice Sheet interpreted from aeromagnetic and radar ice sounding. *Geological Society, London, Special Publications*, *202*(1), 337-355. https://doi.org/10.1144/GSL.SP.2002.202.01.1
4. Blankenship, D. D., Bell, R. E., Hodge, S. M., Brozena, J. M., Behrendt, J. C., & Finn, C. A. (1993). Active volcanism beneath the West Antarctic ice sheet and implications for ice-sheet stability. Nature, 361(6412), 526–529. https://doi.org/10.1038/361526A0
5. Bray, J.R. Surface Albedo Increase following Massive Pleistocene Explosive Eruptions in Western North America. *Quaternary Research*. 1979; 12(2):204-211.doi.10.1016/0033-5894(79)90057-7
6. Chen, J. L., Wilson, C. R., Blankenship, D. D., and Tapley, B. D., Antarctic mass rates from GRACE, *Geophys. Res. Lett.*, 33, L11502 (2006). https://doi.org/10.1029/2006GL026369
7. Coonin, A., Huber, C., Townsend, M., Troch, J., & Scholz, K. (2024). Subglacial Magma Chamber Model with Ice Unloading. Zenodo. https://doi.org/10.5281/zenodo.12188625
8. Corr, H., Vaughan, D. A recent volcanic eruption beneath the West Antarctic ice sheet. *Nature Geosci* **1**, 122–125 (2008). https://doi.org/10.1038/ngeo106
9. W. Degruyter, C. Huber, A model for eruption frequency of upper crustal silicic magma chambers, Earth and Planetary Science Letters, Volume 403, 2014, Pages 117-130, ISSN 0012-821X, https://doi.org/10.1016/j.epsl.2014.06.047.
10. Degruyter, W., Huber, C., Bachmann, O., et al., Influence of exsolved volatiles on reheating silicic magmas by recharge and consequences for eruptive style at Volcán Quizapu (Chile). *Geochemistry, Geophysics, Geosystems*, 18, 4123– 4135 (2017).
11. DIGIS Team, 2023, "2023-12-KAIVCT_ANTARCTICA.csv", GEOROC Compilation: Rift Volcanics, https://doi.org/10.25625/KAIVCT/NSXCRD, GRO.data, V9
12. ETNA, Bulletin Settimanale 26/07/2021-01/08/2021, Rep. N 31/2021, INGV
13. Fretwell, P., Pritchard, H. D., Vaughan, D. G., Bamber, J. L., Barrand, N. E., Bell, R., Bianchi, C., Bingham, R. G., Blankenship, D. D., Casassa, G., Catania, G., Callens, D., Conway, H., Cook, A. J., Corr, H. F. J., Damaske, D., Damm, V., Ferraccioli, F., Forsberg, R., Fujita, S., Gim, Y., Gogineni, P., Griggs, J. A., Hindmarsh, R. C. A., Holmlund, P., Holt, J. W., Jacobel, R. W., Jenkins, A., Jokat, W., Jordan, T., King, E. C., Kohler, J., Krabill, W., Riger-Kusk, M., Langley, K. A., Leitchenkov, G., Leuschen, C., Luyendyk, B. P., Matsuoka, K., Mouginot, J., Nitsche, F. O., Nogi, Y., Nost, O. A., Popov, S. V., Rignot, E., Rippin, D. M., Rivera, A., Roberts, J., Ross, N., Siegert, M. J., Smith, A. M., Steinhage, D., Studinger, M., Sun, B., Tinto, B. K., Welch, B. C., Wilson, D., Young, D. A., Xiangbin, C., and Zirizzotti, A.: Bedmap2: improved ice bed, surface and thickness datasets for Antarctica, The Cryosphere, 7, 375–393, https://doi.org/10.5194/tc-7-375-2013, 2013.

14. A. Geyer, A. Di Roberto, J.L. Smellie, M. Van Wyk de Vries, K.S. Panter, A.P. Martin, J.R. Cooper, D. Young, M. Pompilio, P.R. Kyle, D. Blankenship, Volcanism in Antarctica: An assessment of the present state of research and future directions, Journal of Volcanology and Geothermal Research, Volume 444, 2023, 107941, ISSN 0377-0273, https://doi.org/10.1016/j.jvolgeores.2023.107941.
15. Ghiorso, M.S., Gualda, G.A.R., An H_2O–CO_2 mixed fluid saturation model compatible with rhyolite-MELTS. Contrib Mineral Petrol 169, 53 (2015). https://doi.org/10.1007/s00410-015-1141-8
16. Gomez, N., Pollard, D. & Holland, D. Sea-level feedback lowers projections of future Antarctic Ice-Sheet mass loss. *Nat Commun* **6**, 8798 (2015). https://doi.org/10.1038/ncomms9798
17. Gomez, N., Weber, M.E., Clark, P.U. *et al.* Antarctic ice dynamics amplified by Northern Hemisphere sea-level forcing. *Nature* **587**, 600–604 (2020). https://doi.org/10.1038/s41586-020-2916-2
18. Giordano, G., Lucci, F., Phillips, D. *et al.,* Stratigraphy, geochronology and evolution of the Mt. Melbourne volcanic field (North Victoria Land, Antarctica). *Bull Volcanol* 74, 1985–2005 (2012). https://doi.org/10.1007/s00445-012-0643-8
19. Gualda, G.A.R., Ghiorso, M.S., et al., Rhyolite-MELTS: A Modified Calibration of MELTS Optimized for Silica-rich, Fluid-bearing Magmatic Systems, *Journal of Petrology*, Volume 53, Issue 5, Pages 875–890 (2012). https://doi.org/10.1093/petrology/egr080
20. Handler, P. The effect of volcanic aerosols on global climate, *Journal of Volcanology and Geothermal Research*, Volume 37, Issues 3–4, 1989, Pages 233-249. https://doi.org/10.1016/0377-0273(89)90081-4
21. Hogg, A.E., Gilbert, L., Shepherd, A., Muir, A.S., McMillan, M. Extending the record of Antarctic ice shelf thickness change, from 1992 to 2017, *Advances in Space Research*, Volume 68, Issue 2, 2021, Pages 724-731, ISSN 0273-1177, https://doi.org/10.1016/j.asr.2020.05.030.
22. Huppert, H., Woods, A. The role of volatiles in magma chamber dynamics. Nature 420, 493–495 (2002). https://doi.org/10.1038/nature01211
23. Huybers K, Roe G, Conway H. Basal topographic controls on the stability of the West Antarctic ice sheet: lessons from Foundation Ice Stream. *Annals of Glaciology*. 2017;58(75pt2):193-198. doi:10.1017/aog.2017.9
24. Huybers, P., Langmuir, C., Feedback between deglaciation, volcanism, and atmospheric CO2, *Earth and Planetary Science Letters*, Volume 286, Issues 3–4, Pages 479-491 (2009). https://doi.org/10.1016/j.epsl.2009.07.014
25. Jull, M., and McKenzie, D. (1996), The effect of deglaciation on mantle melting beneath Iceland, *J. Geophys. Res.*, 101(B10), 21815– 21828, doi:10.1029/96JB01308
26. Kim, J., Jung-Woo Park, J.W., et al., Evolution of Alkalic Magma Systems: Insight from Coeval Evolution of Sodic and Potassic Fractionation Lineages at The Pleiades Volcanic Complex, Antarctica, *Journal of Petrology*, Volume 60, Issue 1, Pages 117–150 (2019). https://doi.org/10.1093/petrology/egy108
27. LeMasurier, W.E.; Thomson, J.W.; Baker, P.E.; Kyle, P.R.; Rowley, P.D.; Smellie, J.L.; Verwoerd, W.J.., *Volcanoes of the Antarctic Plate and Southern Ocean.* Washington, D.C., American Geophysical Union, Antarctic Research Series, 48, (1990). https://doi.org/10.1029/AR048

28. LeMasurier, W.E., Choi, S.H., Kawachi, Y. *et al.* Evolution of pantellerite-trachyte-phonolite volcanoes by fractional crystallization of basanite magma in a continental rift setting, Marie Byrd Land, Antarctica. *Contrib Mineral Petrol* 162, 1175–1199 (2011). https://doi.org/10.1007/s00410-011-0646-z
29. LeMasurier, W, Shield volcanoes of Marie Byrd Land, West Antarctic rift: oceanic island similarities, continental signature, and tectonic controls. *Bull Volcanol* 75, 726 (2013). https://doi.org/10.1007/s00445-013-0726-1
30. Licht, K. J., Groth, T., Townsend, et al., Evidence for extending anomalous Miocene volcanism at the edge of the East Antarctic craton. *Geophysical Research Letters*, 45, 3009– 3016 (2018). https://doi.org/10.1002/2018GL077237
31. Lisiecki, L.E. and Raymo, M.E., 2005. A Pliocene-Pleistocene stack of 57 globally distributed benthic $\delta^{18}O$ records. *Paleoceanography*, *20*(1).
32. Liu, Y. et al. Solubility of H2O in rhyolitic melts at low pressures and a new empirical model for mixed H2O–CO2 solubility in rhyolitic melts, Journal of Volcanology and Geothermal Research, 143, 219–235 (2005). https://doi.org/10.1016/j.jvolgeores.2004.09.019
33. Lowenstern, J.B., Carbon dioxide in magmas and implications for hydrothermal systems, Mineralium Deposita, 36: 490-502 (2001). https://doi.org/10.1007/s001260100185
34. Maclennan, J., Jull, M., McKenzie, D., Slater, L., and Grönvold, K., The link between volcanism and deglaciation in Iceland, *Geochem. Geophys. Geosyst.*, 3(11), 1062, doi:10.1029/2001GC000282, 2002.
35. Mixon, E.E., Singer, B.S., Jicha, B.R. and Ramirez, A., 2021. Calbuco, a monotonous andesitic high-flux volcano in the Southern Andes, Chile. *Journal of Volcanology and Geothermal Research*, *416*, p.107279.
36. Möller, R., Dagsson-Waldhauserova, P., Möller, M., Kukla, P.A., Schneider, C., Gudmundsson, M.T. Persistent albedo reduction on southern Icelandic glaciers due to ashfall from the 2010 Eyjafjallajökull eruption, Remote Sensing of Environment, Volume 233, 2019, 111396, https://doi.org/10.1016/j.rse.2019.111396.
37. David Mora, D. and Tassara, A. Upper crustal decompression due to deglaciation-induced flexural unbending and its role on post-glacial volcanism at the Southern Andes, *Geophysical Journal International*, Volume 216, Issue 3, March 2019, Pages 1549-1559, https://doi.org/10.1093/gji/ggy473
38. Moreno-Yaeger, P., Singer, B.S., Jicha, B.R., Nachlas, W.O., Fustos-Toribio, I., Vasquez Antipan, D. (2022) Evolution of magma storage conditions spanning the last glacial-interglacial transition, Mocho-Choshuenco Volcanic Complex, Chile. American Geophysical Union Fall Meeting Abstracts, V13A-02.
39. Moussallam Y., Oppenheimer C., et al., Tracking the changing oxidation state of Erebus magmas, from mantle to surface, driven by magma ascent and degassing, *Earth and Planetary Science Letters*, Volume 393, Pages 200-209, (2014). https://doi.org/10.1016/j.epsl.2014.02.055
40. Oppenheimer, C., Bruno Scaillet, B., Martin, R.S.; Sulfur Degassing from Volcanoes: Source Conditions, Surveillance, Plume Chemistry and Earth System Impacts. *Reviews in Mineralogy and Geochemistry* 2011; 73 (1): 363–421. doi: https://doi.org/10.2138/rmg.2011.73.13

41. Rawson, H., David M. Pyle, D., et al., The magmatic and eruptive response of arc volcanoes to deglaciation: Insights from southern Chile, *Geology*, 44 (4): 251–254 (2016). https://doi.org/10.1130/G37504.1
42. Reading, A.M., Stål, T., Halpin, J.A. et al. Antarctic geothermal heat flow and its implications for tectonics and ice sheets. Nat Rev Earth Environ 3, 814–831 (2022). https://doi.org/10.1038/s43017-022-00348-y.
43. Rocchi, S., Armienti, P., D'Orazio, M., et al., Cenozoic magmatism in the western Ross Embayment: Role of mantle plume versus plate dynamics in the development of the West Antarctic Rift System, *J. Geophys. Res.*, 107(B9), 2195 (2002). https://doi.org/10.1029/2001JB000515
44. Satow, C., Gudmundsson, A., Gertisser, R. *et al.* Eruptive activity of the Santorini Volcano controlled by sea-level rise and fall. *Nat. Geosci.* 14, 586–592 (2021). https://doi.org/10.1038/s41561-021-00783-4
45. Sigmundsson et al., 2010. Climate effects on volcanism: influence on magmatic systems of loading and unloading from ice mass variations, with examples from Iceland. *Phil. Trans. R. Soc. A.,* 3682519–2534 https://doi.org/10.1098/rsta.2010.0042
46. Scholz, K., Townsend, M., Huber, C., Troch, J., Bachmann, O., & Coonin, A. N. (2023). Investigating the impact of an exsolved H_2O-CO_2 phase on magma chamber growth and longevity: A thermomechanical model. *Geochemistry, Geophysics, Geosystems*, 24, e2023GC011151. https://doi.org/10.1029/2023GC011151
47. Schroeder, D.M., Blankenship, D.D., Young, D.A., Quartini. E., Evidence for elevated and spatially variable geothermal flux beneath the West Antarctic Ice Sheet, Proceedings of the National Academy of Sciences, 111 (25) 9070-9072 (2014). https://doi.org/10.1073/pnas.1405184111
48. Shapiro, N. M., & Ritzwoller, M. H. (2004). Inferring surface heat flux distributions guided by a global seismic model: particular application to Antarctica. *Earth and Planetary Science Letters*, *223*(1-2), 213-224. https://doi.org/10.1016/j.epsl.2004.04.011
49. Singer, B.S., Jicha, B.R., Harper, M.A., Naranjo, J.A., Lara, L.E. and Moreno-Roa, H., 2008. Eruptive history, geochronology, and magmatic evolution of the Puyehue-Cordón Caulle volcanic complex, Chile. *Geological Society of America Bulletin*, *120*(5-6), pp.599-618.
50. Smellie, J. L., & Edwards, B. R. (2016). *Glaciovolcanism on Earth and Mars*. Cambridge University Press.
51. Spiegel, C., *et al*., Tectonomorphic evolution of Marie Byrd Land – Implications for Cenozoic rifting activity and onset of West Antarctic glaciation, Global and Planetary Change, Volume 145 (2016). https://doi.org/10.1016/j.gloplacha.2016.08.013
52. Stevens, C., Hulbe, C., Brewer, M., Stewart, C., Robinson, N., Ohneiser, C., et al. (2020). Ocean mixing and heat transport processes observed under the ross ice shelf control its basal melting. *Proc. Natl. Acad. Sci. U.S.A*. 117, 16799–16804. doi: 10.1073/pnas.1910760117
53. Sutter, J., Jones, A., Frölicher, T.L. *et al.* Climate intervention on a high-emissions pathway could delay but not prevent West Antarctic Ice Sheet demise. *Nat. Clim. Chang.* **13**, 951–960 (2023). https://doi.org/10.1038/s41558-023-01738-w
54. Townsend, M., Huber, C., Degruyter, W., Bachmann, O., Magma chamber growth during intercaldera periods: Insights from thermo-mechanical modeling with applications to

Laguna del Maule, Campi Flegrei, Santorini, and Aso. *Geochemistry, Geophysics, Geosystems*, 20, 1574– 1591 (2019).

55. Maximillian van Wyk de Vries, Robert G. Bingham, Andrew S. Hein, 2018. "A new volcanic province: an inventory of subglacial volcanoes in West Antarctica", Exploration of Subsurface Antarctica: Uncovering Past Changes and Modern Processes, M. J. Siegert, S. S. R. Jamieson, D. A. White, https://doi.org/10.1144/SP461.7
56. Watt, S.F., Pyle, D.M. and Mather, T.A., 2013. The volcanic response to deglaciation: Evidence from glaciated arcs and a reassessment of global eruption records. *Earth-Science Reviews*, *122*, pp.77-102.
57. Wilson, A.M., Russell, J.K. Glacial pumping of a magma-charged lithosphere: A model for glaciovolcanic causality in magmatic arcs, *Earth and Planetary Science Letters*, 548, 116500 (2020). https://doi.org/10.1016/j.epsl.2020.116500